**Atmospheric
Chemistry
and Physics
Discussions**

Effects of internal mixing and aggregate morphology on optical properties of black carbon using a discrete dipole approximation model

B. Scarnato[1,2,*], S. Vahidinia[3], D. T. Richard[4], and T. W. Kirchstetter[5,6]

[1]Bay Area Environmental Research Institute, Sonoma, CA, USA
[2]NASA Ames Research Center, Moffett Field, California, USA
[3]Oak Ridge Associated Universities, NASA Ames Research Center, MS 245-5, Moffett Field, CA 94035-1000, USA
[4]Lawrence Livermore National Laboratory, 7000 East Ave, Livermore, CA 94550, USA
[5]Environmental Energy Technologies Division, Lawrence Berkeley National Laboratory, Berkeley, CA 94720, USA
[6]Department of Civil and Environmental Engineering, University of California, Berkeley, CA 94720-1710, USA
[*]currently at: Dept. of Meteorology, Naval Postgraduate School, Monterey, CA 93943, USA

Title Page

Abstract	Introduction
Conclusions	References
Tables	Figures

|◀ | ▶|
| ◀ | ▶ |

Back | Close

Full Screen / Esc

Printer-friendly Version

Interactive Discussion

ACPD

12, 26401–26434, 2012

Effect of internal mixing on optical properties of black carbon aggregates

B. Scarnato et al.

Title Page

Abstract	Introduction
Conclusions	References
Tables	Figures

Back | Close

Full Screen / Esc

Printer-friendly Version

Interactive Discussion

Abstract

According to recent studies, internal mixing of black carbon (BC) with other aerosol materials in the atmosphere alters its aggregate shape, absorption of solar radiation, and radiative forcing. These mixing state effects are not yet fully understood. In this study, we characterize the morphology and mixing state of bare BC and BC internally mixed with sodium chloride (NaCl) using electron microscopy and examine the sensitivity of optical properties to BC mixing state and aggregate morphology using a discrete dipole approximation model (DDSCAT). DDSCAT predicts a higher mass absorption coefficient, lower single scattering albedo (SSA), and higher absorption Angstrom exponent (AAE) for bare BC aggregates that are lacy rather than compact. Predicted values of SSA at 550 nm range between 0.18 and 0.27 for lacy and compact aggregates, respectively, in agreement with reported experimental values of 0.25 ± 0.05. The variation in absorption with wavelength does not adhere precisely to a power law relationship over the 200 to 1000 nm range. Consequently, AAE values depend on the wavelength region over which they are computed. In the 300 to 550 nm range, AAE values ranged in this study from 0.70 for compact to 0.95 for lacy aggregates. The SSA of BC internally mixed with NaCl (100–300 nm in radius) is higher than for bare BC and increases with the embedding in the NaCl. Internally mixed BC SSA values decrease in the 200–400 nm wavelength range, a feature also common to the optical properties of dust and organics. Linear polarization features are also predicted in DDSCAT and are dependent on particle morphology. The bare BC (with a radius of 80 nm) presents in the linear polarization a bell shape feature, which is a characteristic of the Rayleigh regime (for particles smaller than the wavelength of incident radiation). When BC is internally mixed with NaCl (100–300 nm in radius), strong depolarization features for near-VIS incident radiation are evident, such as a decrease in the intensity and multiple modes at different angles corresponding to different mixing states.

DDSCAT, being flexible on the geometry and refractive index of the particle, can be used to study the effect of mixing state and complex morphology on optical properties

of realistic BC aggregates. This study shows that DDSCAT predicts morphology and mixing state dependent optical properties that have been reported previously and are relevant to radiative transfer and climate modeling and interpretation of remote sensing measurements.

1   Introduction

The most recent Intergovernmental Panel on Climate Change report (IPCC, 2007) established that the radiative forcing (RF) of all aerosol types should be estimated in order to understand their effects on the Earth-atmosphere energy budget. The successful accomplishment of this goal requires an accurate parameterization of aerosol optical properties consistent with their physical and chemical proprieties. This study focuses on black carbon (BC), a product of combustion of fossil and biomass fuels, which is the strongest sunlight-absorbing aerosol species (Jacobson, 2001) and a critical component of the global and regional climate (Bond et al., 2004; Bond and Mikhailov, 2005; Ramanathan and Carmichael, 2008).

After emission into the atmosphere, BC becomes increasingly mixed with weak or non-absorbing materials, such as sulfates, nitrates, organics, dust, and sea salt (Mikhailov et al., 2006; Shiraiwa et al., 2007; Xue et al., 2009; Moffet and Prather, 2009; Shiraiwa et al., 2010; Bueno et al., 2011). The absorbing and scattering efficiencies of BC particles, which are aggregates of primary spherules, i.e. monomers, (Tian et al., 2006), depend on primary spherule size, aggregate compactness, and mixing state with other species. Aggregate compactness (fractal dimension) is affected by temperature changes, water, and other aerosol material.

For example, laboratory experiments show that BC aggregates become more compact when embedded in low-viscosity materials, such as glutaric and sulfuric acids (Xue et al., 2009; Zhang et al., 2008). Also, coating BC with non-absorbing compounds, including organic and inorganic acids, leads to an enhancement in light absorption and scattering (e.g., Zhang et al., 2008; Xue et al., 2009; Shiraiwa et al., 2010). Xue et al.

Effect of internal mixing on optical properties of black carbon aggregates

B. Scarnato et al.

Title Page

Abstract	Introduction
Conclusions	References
Tables	Figures

◄◄   ►►

◄   ►

Back   Close

Full Screen / Esc

Printer-friendly Version

Interactive Discussion

CC BY

(2009) found that (i) thin coatings of dicarboxylic acids on BC aggregates enhance light scattering significantly and light absorption slightly and (ii) humidity cycling of glutaric acid coated BC can irreversibly restructure BC aggregates and further modify SSA.

These studies indicate that it is necessary to account for the optical effects of changes to the mixing state and morphology of BC particles when modeling their interaction with sunlight. However, optical properties are not always reproduced by commonly used models, such as Lorenz-Mie-Debye theory (Bohren and Huffman, 1983), Rayleigh-Debye-Gans (RDG) approximation (Zhao and Ma, 2009) and effective medium theory (Bruggeman, 1935; Garnett, 1904). For example, there is a discrepancy between modeled and measured mass absorption coefficient (MAC) for bare BC aggregated (Bond and Bergstrom, 2006; Kahnert, 2010a,b). Bueno et al. (2011) found that the amplification in absorption observed when BC was coated with a surrogate of sulfuric acid was smaller than the predictions using core-shell Mie theory, and they suggested that the discrepancy was due to misrepresentation of the morphology of the coated particles and/or structure of the BC core in the model.

The optics of particles with of complex shapes and refractive index distribution can only be calculated using computational intensive techniques such as T-matrix and discrete dipole approximation (DDA). T-matrix is applicable to homogeneous particles (Mishchenko et al., 1996), while DDA is applicable to both homogeneous particles and with anisotropic composition (Purcell and Pennypacker, 1973; Draine and Flatau, 1994, 2010).

Recent studies show the optical effects of (i) treating bare BC as an aggregation of spherical primary particles rather than as a single sphere (e.g., Liu et al., 2008; Kahnert, 2010b,a; Kahnert and Devasthale, 2011; Wu et al., 2012) and (ii) BC aggregates embedded in other materials (e.g., Liu et al., 2012; Kahnert et al., 2012; Adachi et al., 2010; Liou and Yang, 2011). The studies on bare BC make use of T-matrix, while those on coated BC aggregates make use of core-mantle theory involving two effective medium theories (Liu et al., 2012), finite difference time domain (Wu et al., 2012) in the IR region and DDA (Adachi et al., 2010; Kahnert et al., 2012). Liu et al. (2008) showed

that the relationship between the absorption cross section and the compactness of the BC aggregate is a complex function of the refractive index, the number of monomers, and the monomer size. Further, they found that T-matrix computed optical properties of bare BC aggregates *differ profoundly* from those calculated for the respective volume-equivalent BC spheres and for the respective external mixtures of BC monomers under the assumption that there are no electromagnetic interactions between the monomers. Kahnert and Devasthale (2011) found that the RF at the top of the atmosphere is two times higher if fresh BC is modeled as an aggregate instead of a homogeneous sphere. RF due to aggregates with open chainlike (lacy) structures is 1.1–1.6 times higher than for aggregates with a more compact shape. Adachi et al. (2010) showed that many BC particles from a mega-city have a lacy shapes even after being surrounded by organic matter and that BC is located in offcenter positions within its host material. Off-center embedded BC aggregates absorb sunlight less efficiently than if compact and located near the center of its host particle (Fuller et al., 1999). Further, Adachi et al. (2010) found that RF is 20 % less when modeling internally mixed BC particles as embedded lacy aggregates than as a simple coreshell shape, which is the shape assumed in many climate models.

The impact of shape on aerosol optical properties is a relevant topic as well for interpretation of remote sensing measurements. Any retrieval approach used in analyses of radiometric and polarimetric data requires a model of aerosol particle shape, and in the majority of studies the model of spherical or randomly oriented spheroids particles had been adopted (e.g., Deuze et al., 2001; Hasekamp et al., 2011; Dubovik et al., 2011). Mishchenko and Travis (1997a,b) related the possibility of improvement of satellite aerosol retrievals with use of spectral multi-angular polarization as well as intensity of reflected sunlight. The amount of light escaping the top of the atmosphere is affected by the angle at which the light is reflected by the surface or atmosphere. The MISR sensor on the Terra satellite uses this dependency to separate the aerosol signal from that of surface reflectance and determines the aerosol properties (Kaufman et al., 2002). Polarization of the scattered sunlight is extremely sensitive to such

properties of aerosols as particle size relative to the wavelength and refractive index, which often makes possible the retrieval of these parameters from polarimetric observations (Dlugach and Mishchenko, 2005, 2008). It is known that linear polarization is strongly dependent on particle shape (e.g., Mishchenko et al., 1996, 2002; Wu et al.,
5 2012). It should, therefore, be expected that particle non-sphericity can affect the retrieval of aerosol micro-physical characteristics such as refractive index and size from remote-sensing data.

This paper describes a sensitivity study on the effects of aggregation and internal mixing on optical properties BC, including absorption, scattering, AAE, linear polariza-
10 tion, scattering phase function, and others. We applied a DDA model to examine these effects for black carbon particles bare and mixed with salt that we characterized with scanning and transmission electron microscopes. The discrete dipole approximation model presented captures complexities in particle morphology that other models do not and thus may be useful in predicting aerosol optical properties in climate modeling
15 and interpreting data remotely measured with satellites.

2 Methods

2.1 Particle generation and morphological characterization

We generated bare BC and BC internally mixed with NaCl. We chose NaCl because is an atmospherically abundant inorganic compound derived from evaporated ocean
20 water. Bare BC was generated by nebulizing and drying a stable suspension of BC in pure water. The BC was made with a non-premixed methane-air flame (Kirchstetter and Novakov, 2007). The BC from this flame has a morphology and mass absorption cross-section $8.5\,m^2\,g^{-1}$ at 550 nm, consistent with freshly emitted particles observed in the atmosphere (Moosmuller et al., 2009; Bond and Bergstrom, 2006). Aqueous
25 suspensions of the flame-BC were prepared after its collection on Teflon filters and exposure to ozone, which transformed the BC from a hydrophobic to a hydrophilic state

(Chughtai, 1991), and after which the BC readily mixed with water. To generate coated BC, we dissolved NaCl in the BC suspension and co-nebulized both species together.

The mixing state and morphology of the aerosol mixture was determined using scanning and transmission electron microscopy (SEM and TEM). SEM and TEM images provided morphological information, including aggregate shape, number and size of monomers, and state of mixing with NaCl. We used these images to model aggregates with the same characteristics in the DDA model.

2.1.1 Morphological characterization of aggregates

BC particles can be characterized as a mass fractal, where each particle is represented as an aggregate of the same sized primary spherical particles (monomers), with the following formula

$$N_{\mathrm{m}} = k_0 (R_{\mathrm{g}}^{\mathrm{3D}} / r_{\mathrm{m}})^{D_{\mathrm{f}}} \qquad (1)$$

where N_{m} is the number of monomers, k_0 is the prefactor (structural coefficient), $R_{\mathrm{g}}^{\mathrm{3D}}$ is the three dimensional radius of Gyration, r_{m} is the monomer radius, and D_{f} is the mass fractal dimension. Techniques involving transmission/scanning electron microscopy coupled with digital image analysis have found use in determining D_{f} of aggregates from their projected images. Several studies have suggested that $R_{\mathrm{g}}^{\mathrm{3D}}$ can be extracted by measuring the projected parameters $L_{\mathrm{max}}^{\mathrm{2D}}$. Brasil et al. (1999) suggested a ratio of $L_{\mathrm{max}}^{\mathrm{2D}} / R_{\mathrm{g}}^{\mathrm{3D}} = 3.00 \pm 0.1$ for all N_{m} and overlap factors. D_{f} can be extracted from an empirical statistical scaling power law that relates the size of the aggregate to the ratio $L_{\mathrm{max}}^{\mathrm{2D}} / r_{\mathrm{m}}$:

$$\log(N_{\mathrm{proj}}) = \log(k_0) + D_{\mathrm{f}} \log(R_{\mathrm{g}}^{\mathrm{3D}} / r_{\mathrm{m}}) = \qquad (2)$$

$$\log(k_0) + D_{\mathrm{f}} \log(L_{\mathrm{max}}^{\mathrm{2D}} / 3 r_{\mathrm{m}}) \qquad (3)$$

where the projected number of monomers (N_{proj}) in Eq. (2) is determined from the ratio of the aggregate projected area A_{agg} to the average monomer area A_{p}. An empirical

formula relating N_m and N_{proj} is proposed by Chakrabarty et al. (2011), where N_m can be corrected for an overlapping factor:

$$N_m/N_{proj} = 0.46e^{0.68D_f} \tag{4}$$

The described technique has the advantage of extracting a D_f value independent of the value assumed for k_0. The literature shows a wide range of values for k_0 (Brasil et al., 1999), and it is still under discussion which is most appropriate despite the common use of $k_0 = 1.19$. In Eq. (4), the D_f value of 1.8 has been used.

3 Discrete dipole approximation model

Using the equations above and the morphological features in SEM and TEM images, we constructed model aggregates (targets) to initialize the DDA model, DDSCAT.7 (Draine and Flatau, 1994, 2010). DDSCAT approximates a continuum medium with a finite array of dipoles with individual polarizabilities. The electromagnetic scattering problem for an incident periodic wave interacting with this array of point dipoles is then solved exactly. The principal advantage of the DDA is that it is completely flexible regarding the geometry of the particle, being limited only by the need to use an interdipole separation d that satisfies the relationship $|m|kd < 1$. We use a $|m|kd < 0.5$ to determine the scattering phase function with accuracy of few percentage, where m is the refractive index of the target material and $k = 2\pi/\lambda$. In DDSCAT, the target effective radius, a_{eff}, is defined as the radius of a sphere with the same volume as the target

$$a_{eff} = (3V/4\pi)^{1/3} \tag{5}$$

$$V = Nd^3 \tag{6}$$

where N is the number of dipoles and V is the volume.

The DDSCAT output variables of interest for this study are:

1. The dimensionless quantity α_i with $i = (1, 2, 3)$

$$\alpha_i = I_i / 0.4 M a_{\text{eff}}^2 \tag{7}$$

$$M = \rho V \tag{8}$$

where I_i is the moment of inertia tensor, ρ is the density, and V is the volume of the modeled aggregate. For a solid sphere, e.g. the case S in our study, $\alpha_i = 1$ with $i = (1, 2, 3)$

2. The absorption, scattering and extinction efficiencies ($Q_{\text{abs, scat, ext}}(\lambda)$) defined as

$$Q_{\text{abs,scat,ext}} = C_{\text{abs,scat,ext}} / \pi a_{\text{eff}}^2 \tag{9}$$

where $C_{\text{abs, scat, ext}}(\lambda)$ are the absorption, scattering and extinction geometrical cross sections.

3. The 4 × 4 Mueller scattering intensity matrix (S_{ij}) with $i, j = (1, 2, 3, 4)$ describing the complete scattering properties of the target for specified scattering directions.

From these variables we calculated:

1. The porosity (P) of the structure of modeled aggregates as defined by Shen et al. (2008)

$$P = 1 - f \tag{10}$$

$$f = [(\alpha_2 + \alpha_3 - \alpha_1)(\alpha_3 + \alpha_1 - \alpha_2)(\alpha_1 + \alpha_2 - \alpha_3)]^{-1/2} \tag{11}$$

where α_i is defined in Eq. (7). The value of P is larger for a lacy aggregate than it is for a compact aggregate. P is introduced because the commonly used D_f is not a good measure of porosity and compactness.

2. The mass absorption coefficient (MAC)

$$\mathrm{MAC} = C_{\mathrm{abs}}/\mathrm{mass}_{\mathrm{BC}} \qquad (12)$$

$$\mathrm{mass}_{\mathrm{BC}} = \rho\frac{4}{3}\pi a_{\mathrm{eff}}^3 \qquad (13)$$

where ρ is the density of BC and a_{eff} is the effective radius.

3. The aerosol absorption Angstrom exponent (AAE) computed from the slope of the linear fit passing though MAC curves (in log-log scale).

$$\mathrm{AAE} = \frac{-\triangle\log(\mathrm{MAC})}{\triangle\log(\lambda)} \qquad (14)$$

where AAE = 1 if MAC $\propto \lambda$, and AAE = 0 if MAC is constant with wavelength. AAE is presented for 3 wavelength regions.

4. The single scattering albedo (SSA)

$$\mathrm{SSA} = Q_{\mathrm{scat}}(\lambda)/Q_{\mathrm{ext}}(\lambda) \qquad (15)$$

5. The scattering phase function (S_{11}) which satisfies the normalization $\frac{1}{2}\int_0^\pi S_{11}(\theta)sin(\theta)\,\mathrm{d}\theta$. The scattering angle, $\theta \in [0,\theta]$, is defined as the angle between the incidence and scattering directions.

6. The degree of linear polarization $-S_{12}(\theta)/S_{11}(\theta)$.

In this study, the refractive index of BC and NaCl is considered constant in the spectral range between 200 and 1000 nm (Moffet and Prather, 2009), where m_{BC} = 1.95–0.79i and m_{NaCl} = 1.5. We assumed a density of BC ρ_{BC} = 1.8 g cm^{-3} (Bond and Bergstrom, 2006). All the computed optical values are averaged for 64 random target orientations and multiple scattering planes and satisfy the condition $|m|kd < 0.5$.

Effect of internal mixing on optical properties of black carbon aggregates

B. Scarnato et al.

Title Page

Abstract	Introduction
Conclusions	References
Tables	Figures

|◄ ►|

◄ ►

| Back | Close |

Full Screen / Esc

Printer-friendly Version

Interactive Discussion

4   Results

4.1   Uncoated BC aggregates

The SEM images in Fig. 1 show the fractal nature of the generated bare BC. The aggregates are composed of spherical primary particles (monomers) of about the same size.
The characteristics of the bare BC studied are presented in Table 1 and Fig. 2. Cases A through E correspond to five types of aggregates that vary in compactness (porosity) and number and size of monomers. Case S is a homogeneous sphere approximation (HSA).

Predicted values of MAC are shown in Fig. 3a. At wavelengths smaller than 550 nm, MAC values depend on the morphology of the BC aggregate. The MAC curves separate in this wavelength range as a result of the dependency between the size of the particle and the incident radiation wavelength. For lager bare BC aggregates, the separation starts at longer wavelengths. (This is also evident in the case of larger coated BC aggregates, as shown in Fig. 7a.) Generally, MAC is characterized by higher values for smaller aggregates (with lower mass). Higher MAC values are found for lacy aggregates compared to more compact structures (this general behavior is also found by Liu et al., 2008 and Kahnert and Devasthale, 2011). Compared to aggregates (cases D and E), the homogeneous sphere approximation (HSA, case S) exhibits significantly lower MAC below 550 nm and slightly higher MAC in the Rayleigh regime (550–1000 nm). In all cases, MAC lies between 6.5 and 7.0 $m^2 g^{-1}$ at 550 nm, in agreement with the range of values reported by Bohren and Huffman (1983); Martins et al. (1998); Fuller et al. (1999); Bergstrom (1973); Bond and Bergstrom (2006); Adachi et al. (2007).

For aggregates with a much larger number of monomers (600) than those modeled in this study, Kahnert (2010b) estimated a MAC values (at 550 nm) of $5.2 \pm 0.1\,m^2 g^{-1}$ for lacy aggregates, $4.9 \pm 0.1\,m^2 g^1$ for compact aggregates, and $3.3 \pm 0.4\,m^2 g^1$ for spheres. These lower values are likely the result of the large number of aggregate monomers, see Eq. (12), where compact aggregates show a low porosity.

Title Page

Abstract | Introduction

Conclusions | References

Tables | Figures

◄ | ►

Back | Close

Full Screen / Esc

Printer-friendly Version

Interactive Discussion

The variation in absorption with wavelength does not adhere precisely to a power law relationship over the 200 to 1000 nm range. Consequently computed AAE values depend on the wavelength range considered. As shown in Table 1, values of AAE values computed between 200 and 550 nm (0.6–0.8) are smaller than those computed between 550 and 1000 nm (0.96 to 1.05). AAE values of $\simeq 1$ in the Rayleigh regime (550–1000 nm) are consistent with observations (e.g., Russell et al., 2010) and other theoretical results (Bohren and Huffman, 1983; Bergstrom, 1973).

Predicted values of AAE were sensitive to aggregate compactness and monomer size. Compact aggregates exhibited lower AAE values than lacy aggregates (compare cases A vs. C and cases D vs. E). Compact aggregates with the same monomer diameter (cases C and E), while having different aggregate size, have lower AAEs than the aggregate with smaller diameter monomers (case B). AAE values are also different for aggregates with the same porosity (cases B and E) but with different numbers of differently sized monomers.

Predicted values of SSA are shown in Fig. 3b. Values of SSA are higher for compact aggregates than for lacy aggregates, in agreement with Kahnert and Devasthale (2011). Compact aggregates are characterized by a higher scattering cross section than lacy aggregates, also found by Liu et al. (2008), due to a stronger scattering interaction and stronger electromagnetic coupling between spherules. The SSA values for BC aggregates and the homogeneous sphere (HSA, case E) differ markedly. The 550 nm SSA for BC aggregates range between 0.18 and 0.27 as a function of compactness and size of the aggregate, in agreement with the suggested value around 0.25 ± 0.05 (Kahnert, 2010b; Fuller et al., 1999), while a much higher SSA of 0.39 is predicted for HSA case.

4.2   BC internally mixed with NaCl

The TEM images in Fig. 4 illustrate different types of internal mixing: (a) total inclusion of BC in NaCl particle, (b) partial inclusion and partial surface contact of BC on NaCl surface, and (c) inclusion of NaCl in a larger BC aggregate. Laskin et al. (2012) present

similar images of NaCl collected during two recent field campaigns. As indicated in Table 2 and Figs. 5 and 6, we simulated these different possibilities: two cases of complete BC inclusion in NaCl (cases FI and GI) and two cases of BC inclusion and surface contact of BC on NaCl (FIS and GIS). For comparison, we also modeled two cases (F and G) of lacy and compact BC aggregates in bare condition (i.e., not mixed with NaCl).

Predicted values of MAC are shown in Fig. 7a. Compared to bare BC aggregates, the MAC of BC mixed with NaCl is substantially larger. The maximum MAC amplification factor (about 2.2–2.7) is found when BC is completely immersed in NaCl (compare cases FI and GI to cases F and G). The compactness of the BC aggregate influenced the MAC of BC-NaCl mixtures. Higher MAC amplification factors are found for internally mixed compact BC (with even less coating amounts) than for internally mixed lacy BC. Compared to bare BC, the MAC of the mixtures increased because of (i) the larger refractive index of the NaCl surrounding the BC (Bohren, 1986; Flanner et al., 2012) and (ii) internal reflections in the non-absorbing NaCl (Fuller et al., 1999). Additionally, radiation is focused near the center of the particle, enabling further absorption enhancement from inclusions that happen to reside near the center of the composite (Bohren, 1986).

In the 550 to 1000 nm region, the AAE for coated particles increases as BC becomes increasingly embedded in NaCl. In the region between 200 and 550 nm, AAE decreases with the increase of embedding of BC in NaCl (see Table 2). As with bare BC, the AAE of BC internally mixed with NaCl is smaller in the 200 to 550 nm range than it is in 550 to 1000 nm range.

Predicted values of SSA are shown in Fig. 7b. The mixing of BC with NaCl amplifies both absorption and scattering, but scattering increases more than absorption and, therefore, SSA increases. For the cases studied, SSA tends to decrease at wavelengths below 400 nm. This feature is a characteristic of the size of this aerosol mixture, and it is a feature also common to the optical properties of dust and organics (Russell et al., 2010).

Title Page

Abstract | Introduction

Conclusions | References

Tables | Figures

◄ | ►

◄ | ►

Back | Close

Full Screen / Esc

Printer-friendly Version

Interactive Discussion

4.3 Scattering phase function and polarization

Scattering phase functions at 466 and 733 nm for bare and coated BC are presented in Fig. 8. The phase function describes how much light is scattered in each direction. The peak of the scattering phase function is connected to the size of the particle, where the bigger the particle the higher is the forward scattered intensity. As shown in Fig. 8, the phase function also depends on aggregate compactness and mixing state. Lacy BC (case F) exhibits a stronger forward scattering intensity than compact BC (case G), which presents a more pronounced backscatter. At both 466 and 773 nm, forward scattering increases when BC is totally embedded in NaCl (compare case F with FI and case G with GI). This effect is much less pronounced when BC is only partially embedded (compare case F with FIS and case G with GIS). At 466 nm, increasing the mixing of BC with NaCl decreases the backscattered intensity (compare case F with FI and FIS and case G with GI and GIS). At 733 nm, scattering phase functions are similar (despite the difference in size) for bare BC and BC particles that are not fully embedded in NaCl (cases F and FIS and cases G and GIS), and a marked reduction in backscatter is evident only when BC is completely embedded in NaCl (cases FI and GI).

The degree of linear polarization, $-S_{12}(\theta)/S_{11}(\theta)$, is shown in Fig. 9. Perfectly polarized radiation has a degree of linear polarization equal to 1, whereas unpolarized radiation has a degree of linear polarization equal to 0. At 466 and 733 nm, the particles with a_{eff} between 82 and 130 nm exhibit bell shape curves (Rayleigh regime), whereas larger particles closer to the radiation wavelength present multiple modes including negative degree of polarization at different angles (depolarization features). This complex structure is characteristic of Mie scattering, and is due to the complex interactions of scattered and refracted rays that result in constructive and destructive interference along different paths (i.e., different scattering angles). The negative sign of degree of linear polarization indicates that the scattered light is polarized parallel to the reference plane, whereas a positive degree of polarization indicates that the light

Title Page

Abstract | Introduction

Conclusions | References

Tables | Figures

◄◄ | ►►

◄ | ►

Back | Close

Full Screen / Esc

Printer-friendly Version

Interactive Discussion

is polarized perpendicular to the reference plane. At 700 nm, depolarization features are evident only for the compact BC with a smaller inclusion of NaCl (case GI), where $-S_{12}(\theta)/S_{11}(\theta)$ shows a negative degree of polarization starting at 60 degrees. This signature is more likely caused by the morphology (greater compactness of the BC aggregate) than overall particle size because, despite being larger, case FI presents a more of a bell shaped curve with less dramatic depolarization features (a peak at 120 instead of 90 degrees). For shorter wavelengths, when size of the particle and wavelengths are more comparable, $-S_{12}(\theta)/S_{11}(\theta)$ shows more complicated features (resonances) with negative degree of polarization also at smaller angles.

5 Summary and discussion

In this study, models of bare and BC internally mixed with NaCl were developed based on SEM and TEM images, and optical properties including MAC, AAE, SSA, scattering phase function, and polarization were predicted over the 200 to 1000 nm range using DDSCAT, which applies the discrete dipole approximation (DDA). DDA is applicable to particles with arbitrary shape and anisotropic composition, which allows computation of optical properties of particles with complex chemistry and morphology, whereas other approaches require unrealistic simplifications such as averaging the refractive indexes of mixed composition particles (like the effective medium theory).

Key results include: (i) lacy aggregates have a higher MAC and lower SSA than compact aggregates, which is consistent with other modeling studies. (ii) Computed MAC are consistent with measured values of $7.5 \pm 1.2 \, \mathrm{m^2 \, g^{-1}}$. The amplification factors of the MAC, attributed to the mixing state of BC with NaCl, vary between 1.2 and 2.7 and are largely independent of wavelength in the visible spectrum: the highest MAC is given for compact aggregates fully embedded in NaCl. (iii) The variation in absorption with wavelength does not adhere precisely to a power law relationship over the 200 to 1000 nm range. Consequently, the AAE depends on the wavelength range over which it is computed. AAE for bare BC aggregates is sensitive to level of compactness and monomer

size, presenting smaller values for compact than lacy aggregates. (iv) Computed values of SSA at 550 nm range between 0.18 and 0.27 for lacy and compact aggregates, respectively, in agreement with reported experimental values of of 0.25 ± 0.05. The SSA of BC internally mixed with NaCl (100–300 nm in radius) is higher than for bare BC and

5 increases with embedding in NaCl. The SSA (of internally mixed BC) decreases in the 200–400 nm wavelength range, a feature common also to the optical properties of dust and organics. (v) The linear polarization of scattered sunlight is strongly dependent on particle shape. Bare BC (with a radius of 80 nm) presents in the linear polarization a bell shape feature, which is a characteristic of the Rayleigh regime. When BC is inter-

10 nally mixed with NaCl (100 and 300 nm in radius), strong depolarization features are evident.

In radiative transfer calculations that are used to interpret space or ground-based observations, various assumptions are made regarding the aerosol optical properties. It is common to approximate aerosol shape by homogeneous spherical or spheroidal

15 particles, ignoring the effect of realistic morphology and mixing with other aerosol compounds. The results of this study indicate that there are significant differences in the optical properties of BC when modeled as an aggregate compared to the equivalent volume sphere (HSA), and in the optical properties of bare BC and internally mixed BC. Therefore, assuming spherical instead of irregularly shaped particles in radiative

20 transfer calculations can lead to significant errors in retrieved atmospheric parameters, such as the aerosol type, optical thickness and particle size distributions, composition, and so forth (see Dlugach and Petrova (2003) for a complete discussion of errors). Similarly, the SSA of BC coated with NaCl exhibits features that are common to the optical properties of dust and organics, which could be misleading when inferring aerosol

25 composition from measurements of SSA. Last, since Jacobson (2000) and others have demonstrated that BC mixing state strongly influences RF, deriving optical properties that are consistent with the complex morphology and mixing state of aerosols is warranted. The DDA model employed in this study, which has not yet been widely applied in climate assessments, may prove useful in addition other more widely used models.

References

Adachi, K., Chung, S., and Busek, F.: Fractal parameters of individual soot particles determinated using electron tomography: implications for optical properties, J. Geophys. Res., 112, 827–849, 2007. 26412

Adachi, K., Chung, S., and Buseck, P.: Shapes of soot aerosol particles and implications for their effects on climate, J. Geophys. Res., 115, D15206, doi:10.1029/2009JD012868, 2010. 26405, 26406

Bergstrom, R.: Extinction and Absorption Coefficients of the Atmospheric Aerosol as a Function of Particle Size, Contr. Atmos. Phys., 46, 223–234, 1973. 26412, 26413

Bohren, C.: Applicability of effective medium theories to problems of scattering and absorption by nonhomogenous atmospheric particles., J. Atmos. Sci., 43, 468–475, 1986. 26414

Bohren, C. F. and Huffman, D. R.: Absorption and Scattering of Light by Small Particles., John Wiley and Sons, New York, NY, USA, 1983. 26405, 26412, 26413

Bond, T. and Bergstrom, R.: Light Absorption by Carbonaceous Particles: An Investigative Review, Aerosol Sci. Tecnol., 40, 27–67, 2006. 26405, 26407, 26411, 26412

Bond, T. and Mikhailov: Can reducing black carbon emissions counteract global warming?, Env. Sci. Technology, 39, 5921–5926, 2005. 26404

Bond, T., Streets, D., Yarber, K., and Nelson, S.: A technology based inventory of black and organic carbon emissions from combustion, J. Geophys. Res., 108, 8823, doi:10.1029/2002JD003117, 2004. 26404

Full Screen / Esc

Printer-friendly Version

Interactive Discussion

Brasil, A. M., Farias, T. L., and Carvalho, M. G.: A Recipe for Image characterization of Fractal-Like Aggregates, J. Aerosol Sci., 30, 1379–1389, 1999. 26408

Bruggeman, D.: Berechnung verschiedener physikalischer Konstanten von heterogenen Substanzen, Ann. Phys. (Leipzig), 636–679, 1935. 26405

Bueno, P. A., Havey, D. K., Mulholland, G. W., Hodges, J. T., Gillis, K. A., Dickerson, R. R., and Zachariah, M. R.: Photoacoustic Measurements of Amplification of the Absorption Cross Section for Coated Soot Aerosols, Aerosol Sci. Technol., 45, 1217–1230, doi:10.1080/02786826.2011.587477, 2011. 26404, 26405

Chakrabarty, R., Garroab, M., Garroabc, B., Chancellorab, S., Moosmullerab, H., and Herald, C.: Simulation of Aggregates with Point-Contacting Monomers in the Cluster-Dilute Regime. Part 1: Determining the Most Reliable Technique for Obtaining Three-Dimensional Fractal Dimension from Two-Dimensional Images, Aerosol Sci. Technol., 45, 75–80, doi:10.1080/02786826.2010.520363, 2011. 26409

Chughtai, A. R., Jassim, J. A., Peterson, J. H., Stedman, D. H., and Smith, D. M.: Spectroscopic and solubility characteristics of oxidized soot, Aerosol Sci. Technol., 15, 112–126, 1991. 26408

Deuze, J., Breon, F., Devaux, C., Goloub, P., Herman, H., Lafrance, B., Maignan, F., Marchand, A., Nadal, F., Perry, G., and Tanre, D.: Remote sensing of aerosols over land surfaces from POLDER-ADEOS-1 polarized measurements, J. Geophys. Res., 106, 4913–4926, doi:10.1029/2000JD900364, 2001. 26406

Dlugach, J. and Mishchenko, M.: Photopolarimetry of planetary atmospheres: what observational data are essential for a unique retrieval of aerosol microphysics?, Monthly Notices of the Royal Astronomical Society, 384, 64–70, 2008. 26407

Dlugach, Z. and Petrova, E.: Polarimetry of Mars in high-transparency periods: How reliable are the estimates of aerosol optical properties?, Solar System Res., 37, 87–100, 2003. 26417

Dlugach, Z. M. and Mishchenko, M. I.: The effect of aerosol shape in retrieving optical properties of cloud particles in the planetary atmospheres from the photopolarimetric data, Jupiter, Solar System Research, 39, 102–111, doi:10.1007/s11208-005-0026-1, 2005. 26407

Draine, B. and Flatau, P. J.: Discrete dipole approximation for scattering calculations, J. Opt. Soc. Am. A, 11, 1491–1499, 1994. 26405, 26409

Draine, B. and Flatau, P. J.: User Guide to the Discrete Dipole Approximation Code DDSCAT 7.1, 2010. 26405, 26409

Effect of internal mixing on optical properties of black carbon aggregates

B. Scarnato et al.

Dubovik, O., Herman, M., Holdak, A., Lapyonok, T., Tanré, D., Deuzé, J. L., Ducos, F., Sinyuk, A., and Lopatin, A.: Statistically optimized inversion algorithm for enhanced retrieval of aerosol properties from spectral multi-angle polarimetric satellite observations, Atmos. Meas. Tech., 4, 975–1018, doi:10.5194/amt-4-975-2011, 2011. 26406

5 Flanner, M. G., Liu, X., Zhou, C., Penner, J. E., and Jiao, C.: Enhanced solar energy absorption by internally-mixed black carbon in snow grains, Atmos. Chem. Phys., 12, 4699–4721, doi:10.5194/acp-12-4699-2012, 2012. 26414

Fuller, K. A., Malm, W. C., and Kreidenweis, S. M.: Effects of mixing on extinction by carbonaceous particles, J. Geophys. Res., 104, 15941–15954, 1999. 26406, 26412, 26413, 26414

10 Garnett, J.: Colours in metal glasses and in metallic films, Philos. Trans. Roy. Soc. Lond., 385–420, 1904. 26405

Hasekamp, O., Litvinov, P., and Butz, A.: Aerosol properties over the ocean from PARASOL multiangle photopolarimetric measurements, J. Geophys. Res., 116, D14204, doi:10.1029/2010JD015469, 2011. 26406

15 IPCC: Climate Change 2007: The Physical Science Basis. Summary for Policy Makers, 2007. 26404

Jacobson, M.: A physically-based treatment of elemental carbon optics: Implications for global direct forcing of aerosol, Geophys. Res. Lett., 27, 217–220, 2000. 26417

Jacobson, M.: Strong radiative heating due to mixing state of black carbon in atmospheric
20 aerosol, Letters to Nature, 409, 695–697, 2001. 26404

Kahnert, M.: On the Discrepancy between Modeled and Measured Mass Absorption Cross Sections of Light Absorbing Carbon Aerosols, Aerosol Sci. Technol., 44, 453–460, doi:10.1080/02786821003733834, 2010a. 26405

Kahnert, M.: Numerically exact computation of the optical properties of light absorbing car-
25 bon aggregates for wavelength of 200 nm–12.2 µm, Atmos. Chem. Phys., 10, 8319–8329, doi:10.5194/acp-10-8319-2010, 2010b. 26405, 26412, 26413

Kahnert, M. and Devasthale, A.: Black carbon fractal morphology and short-wave radiative impact: a modelling study, Atmos. Chem. Phys., 11, 11745–11759, doi:10.5194/acp-11-11745-2011, 2011. 26405, 26406, 26412, 26413

30 Kahnert, M., Nousiainen, T., Lindqvist, H., and Ebert, M.: Optical properties of light absorbing carbon aggregates mixed with sulfate: assessment of different model geometries for climate forcing calculations, Opt. Express, 20, 10042–10058, doi:10.1364/OE.20.010042, 2012. 26405

Effect of internal mixing on optical properties of black carbon aggregates

B. Scarnato et al.

Title Page

Abstract	Introduction
Conclusions	References
Tables	Figures

◄◄   ►►

◄   ►

Back   Close

Full Screen / Esc

Printer-friendly Version

Interactive Discussion

Kaufman, Y., Tanre, D., and Boucher, O.: A satellite view of aerosols in the climate system, Nature, 419, 215–223, 2002. 26406

Kirchstetter, T. and Novakov, T.: Controlled generation of black carbon particles from a diffusion flame and applications in evaluating black carbon measurement methods, Atmos. Environ., 41, 1874–1888, 2007. 26407

Laskin, A., Moffet, R., Gilles, M. K., Fast, J. D., Zaveri, R. A., Wang, B., Nigge, P., and Shutthanandan, J.: Tropospheric Chemistry of Internally Mixed Sea Salt and Organic Particles: Surprising Reactivity of NaCl with Weak Organic Acids, J. Geophys. Res., 117, D15302, doi:10.1029/2012JD017743, 2012. 26413

Liou, K. N., Takano, Y., and Yang, P.: Light absorption and scattering by aggregates: Application to black carbon and snow grains, J. Quant. Spec. Ra. Transfer., 112, 1581–1594, 2011. 26405

Liu, C., Panetta, R. L., and Yang, P.: The Influence of Water Coating on the Optical Scattering Properties of Fractal Soot Aggregates, Aerosol Sci. Technol., 46, 31–43, doi:10.1080/02786826.2011.605401, 2012. 26405

Liu, L., Mishchenko, M. I., and Arnott, W. P.: A study of radiative properties of fractal soot aggregates using the superposition T-matrix method, J. Quant. Spec. Ra. Transfer., 109, 2656–2663, 2008. 26405, 26412, 26413

Martins, J., Artaxo, P., Liousse, C., Reid, J. S., Hobbs, P. V., and J., K. Y.: Effects of black carbon content, particle size, and mixing on light absorption by aerosols from biomass burning in Brazil, J. Geophys. Res., 103, 32041–32050, doi:10.1029/98JD02593, 1998. 26412

Mikhailov, E. F., Vlasenko, S. S., Podgorny, I. A., Ramanathan, V., and Corrigan, C. E.: Optical proprieties of soot water drop agglomerates: an experimental study, J. Geophys. Res., 111, D07209, doi:10.1029/2005JD006389, 2006. 26404

Mishchenko, M., Travis, L. D., and Lacis, A. A.: Scattering, Absorption, and Emission of Light by Small Particles, Cambridge University Press, Cambridge, 2002. 26407

Mishchenko, M. I. and Travis, L.: Satellite retrieval of aerosol properties over the ocean using polarization as well as intensity of reflected sunlight, J. Geophys. Res., 102, 16989–17013, 1997a. 26406

Mishchenko, M. I. and Travis, L. D.: Satellite retrieval of aerosol properties over the ocean using measurements of reflected sunlight: Effect of instrumental errors and aerosol absorption, J. Geophys. Res., 13543–13553, 1997b. 26406

Effect of internal mixing on optical properties of black carbon aggregates

B. Scarnato et al.

Mishchenko, M. I., Travis, L. D., and Mackowski, D. W.: T-matrix computations of light scattering by nonspherical particles: A review, J. Quant. Spec. Ra. Transfer., 55, 535–575, doi:10.1016/0022-4073(96)00002-7, 1996. 26405, 26407

Moffet, R. and Prather, K.: In-situ measurements of the mixing state and optical properties of soot with implications for radiative forcing estimates, P. Natl. Acad. Sci., 106, 11872–11877, 2009. 26404, 26411

Moosmuller, H., Chakrabarty, R., and Arnott, W.: Aerosol light absorption and its measurement: A review, J. Quant. Spec. Ra. Transfer., 110, 844–878, doi:10.1016/j.jqsrt.2009.02.035, 2009. 26407

Purcell, E. and Pennypacker, C.: Scattering and Absorption of Light by Nonspherical Dielectric Grains, The Astrophysical Journal, 186, 705–714, doi:10.1086/152538, 1973. 26405

Ramanathan, V. and Carmichael, G. R.: Global and regional climate changes due to BC, Nature, 1, 221–227, 2008. 26404

Russell, P. B., Bergstrom, R. W., Shinozuka, Y., Clarke, A. D., DeCarlo, P. F., Jimenez, J. L., Livingston, J. M., Redemann, J., Dubovik, O., and Strawa, A.: Absorption Angstrom Exponent in AERONET and related data as an indicator of aerosol composition, Atmos. Chem. Phys., 10, 1155–1169, doi:10.5194/acp-10-1155-2010, 2010. 26413, 26414

Shen, Y., Draine, B. T., and Eric, T. J.: Modeling Porous Dust Grains with Ballistic Aggregates. I. Geometry and Optical Properties, The Astrophysical Journal, 689, 260, http://stacks.iop.org/0004-637X/689/i=1/a=260, 2008. 26410

Shiraiwa, M., Kondo, Y., Moteki, N., Takegawa, N., Miyazaki, Y., and Blake, D. R.: Evolution of Mixing State of Black Carbon in Polluted Air from Tokyo, Geophys. Res. Lett., 34, L16803, doi:10.1029/2007GL029819, 2007. 26404

Shiraiwa, M., Kondo, Y., Iwamoto, T., and Kita, K.: Amplification of Light Absorption of Black Carbon by Organic Coating, Aerosol Sci. Technol., 44, 46–54, doi:10.1080/02786820903357686, 2010. 26404

Tian, K., Thomson, K., Liu, F., Snelling, D., Smallwood, G., and Wang, D.: Determination of the morphology of soot aggregates using the relative optical density method for the analysis of TEM images, Combustion and Flame, 144, 782–791, doi:10.1016/j.combustflame.2005.06.017, 2006. 26404

Wu, Y., Gu, X., Cheng, T., Xie, D., Yu, T., Chen, H., and Guo, J.: The single scattering properties of the aerosol particles as aggregated spheres, J. Quant. Spec. Ra. Transfer., 113, 1454–1466, doi:10.1016/j.jqsrt.2012.03.015, 2012. 26405, 26407

Effect of internal mixing on optical properties of black carbon aggregates

B. Scarnato et al.

Title Page

Abstract	Introduction
Conclusions	References
Tables	Figures

◄ | ►|

◄ | ►

Back | Close

Full Screen / Esc

Printer-friendly Version

Interactive Discussion

Xue, H., Khalizov, A. F., Wang, L., Zheng, J., and Zhang, R.: Effects of dicarboxylic acid coating on the optical properties of soot, Chem. Chem. Phys., 11, 7869–7875, doi:10.1039/B904129J, 2009. 26404

Zhang, R., Khalizov, A. F., Pagels, J., Zhang, D., Xue, H., and McMurry, P. H.: Variability in morphology, hygroscopicity, and optical properties of soot aerosols during atmospheric processing, Proceedings of the National Academy of Sciences, 105, 10291–10296, doi:10.1073/pnas.0804860105, 2008. 26404

Zhao, Y. and Ma, L.: Applicable range of the Rayleigh-Debye-Gans theory for calculating the scattering matrix of soot aggregates, Appl. Opt., 48, 591–597, doi:10.1364/AO.48.000591, 2009. 26405

Title Page

Abstract | Introduction

Conclusions | References

Tables | Figures

⏮ | ⏭

◀ | ▶

Back | Close

Full Screen / Esc

Printer-friendly Version

Interactive Discussion

Table 1. Characteristics of the modeled bare BC and optical properties predicted by DDSCAT.

Case	$2r_m$ [nm]	N_m	a_{eff} [nm]	P	AAE (200–550 nm)	AAE (288–550 nm)	AAE (550–1000 nm)
A	40	70	82	0.84	0.83	0.88	1.04
B	30	64	60	0.80	0.86	0.95	1.05
C	40	70	82	0.72	0.62	0.77	1.01
D	40	100	100	0.92	0.76	0.85	1.02
E	40	100	100	0.80	0.59	0.70	0.96
S	N/A	N/A	100	0	0.08	0.01	1.04

Title Page

Abstract | Introduction

Conclusions | References

Tables | Figures

|◄ | ►|

◄ | ►

Back | Close

Full Screen / Esc

Printer-friendly Version

Interactive Discussion

Table 2. Characteristics of the modeled bare BC and mixtures of BC and NaCl and optical properties predicted by DDSCAT. The core BC has 70 monomers with diameter of 40 nm.

Cases	a_{eff} [nm]	P	$V_{\text{NaCl}}/V_{\text{BC}}$ $(a_{\text{eff, shell}}/a_{\text{eff, core}})$	AAE (200–550 nm)	AAE (288–550)	AAE (550–1000 nm)
F	82	0.86	–	0.73	0.86	1.00
G	82	0.60	–	0.53	0.68	1.00
FI	303		50 (3.7)	0.58	0.75	1.13
GI	199		9.17 (2.42)	0.40	0.58	1.27
FIS	138		4.47 (1.68)	0.74	0.83	1.15
GIS	110		0.84 (1.34)	0.38	0.54	1.14

MACS4800 2.0kV-D 4.2mm x80.0k SE(M,LA1) 3/11/2011 500nm

MACS4800 2.0kV-D 4.2mm x80.0k SE(M,LA1) 3/11/2011 500nm

(a)   (b)

Fig. 1. Two SEM images both showing heterogeneity in the morphology of the bare BC aggregates, illustrating "lacy" and "compact" structures.
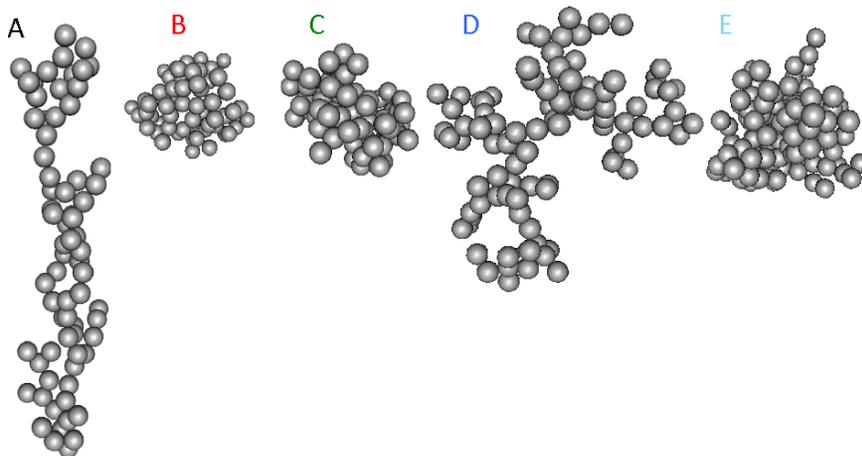
Fig. 2. Visual representation of modeled bare BC. The labels A-E are color coded to match the legends in the Fig. 3. Case A is a lacy structure of 70 monomers with diameters of 40 nm. Case B is a compact structure of 64 monomers with diameters of 30 nm. Case C is a compact version of case A. Cases D and E are aggregates of 100 monomers with diameters of 40 nm, but with different compactness.

Title Page

Abstract | Introduction

Conclusions | References

Tables | Figures

◄ | ►

◄ | ►

Back | Close

Full Screen / Esc

Printer-friendly Version

Interactive Discussion

(a) MAC for bare BC

(b) *SSA for bare BC*

Fig. 3. Spectral dependence of MAC **(a)** and SSA **(b)** for five bare BC aggregates (cases A–E) and one homogeneous sphere approximation with equivalent volume of case D and E (HSA, case S). For a fixed number of the same sized monomers, compact aggregates exhibit lower MAC and higher SSA than lacy aggregates. All the computed optical values are averaged over 64 target orientations and satisfy the condition $|m|kd < 0.5$. We use $m_{BC} = 1.95 - 0.79i$ and $\rho_{BC} = 1.8 \, \mathrm{g\,cm^{-3}}$. The characteristics of the bare BC are described in Table 1 and Fig. 2.
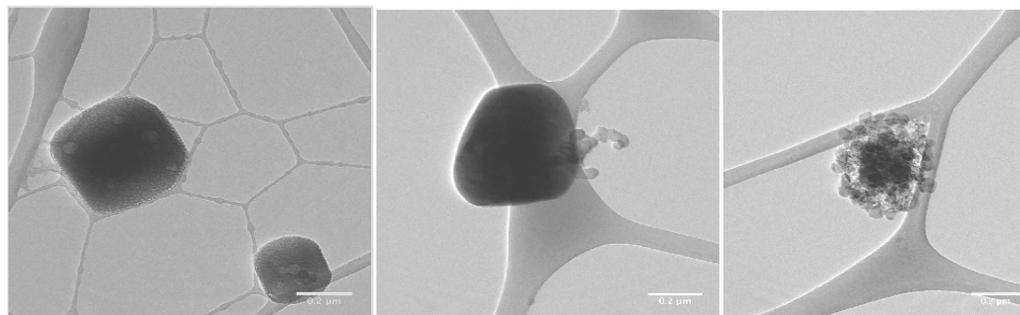
(a) *BC immersion in NaCl*   (b) *BC immersion in and surface contact with NaCl*   (c) *NaCl immersion in BC*

Fig. 4. TEM images of BC (lighter grey) mixed with NaCl (darker grey): **(a)** total inclusion of BC in NaCl, **(b)** partial inclusion and partial surface contact of BC in NaCl, and **(c)** total inclusion of NaCl in BC.

(a) *Bare lacy BC (F)*

(b) *BC partial immersion and partial surface contact on NaCl crystal (FIS)*

(c) *BC immersion on NaCl (FI)*
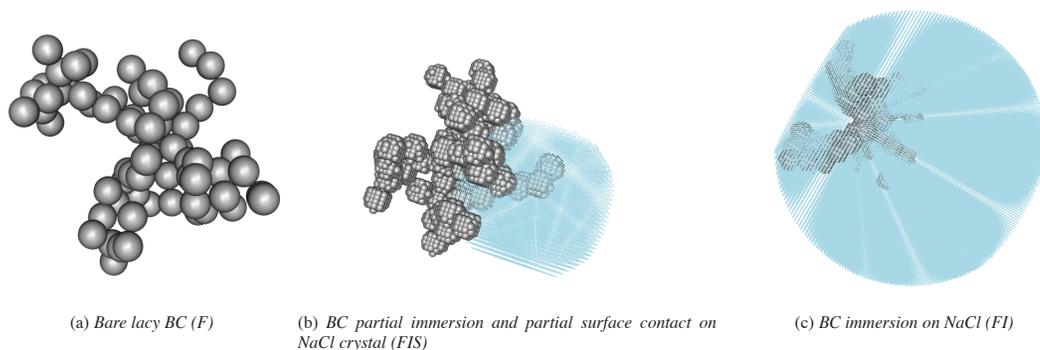
Fig. 5. Visual representation of modeled internal mixtures of lacy BC aggregates and NaCl. **(a)** Case F is a bare lacy BC aggregate. **(b)** Case FIS shows a BC partial immersion and partial surface contact on NaCl crystal, while **(c)** case FI is a total inclusion of BC (lighter grey) in salt particle (light blue). The points in light blue are the dipoles representing NaCl, while the circle in light grey represent the dipole position for BC. The dense number of dipoles finely characterizes the morphology of NaCl and of the BC aggregate.

(a) *Bare compact BC (G)*   (b) *NaCl immersion on BC (GIS)*   (c) *BC immersion on NaCl (GI)*
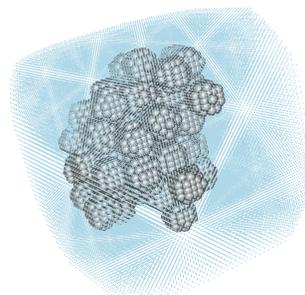
Fig. 6. Visual representation of modeled internal mixtures of compact BC aggregates and NaCl. **(a)** Case G is a bare compact BC aggregate. **(b)** Case GIS shows a compact BC with an "inclusion" of NaCl, while **(c)** case GI is a total inclusion of BC (lighter grey) in salt particle (light blue). The points in light blue are the dipoles representing NaCl, while the circle in light grey represent the dipole position for BC. The dense number of dipoles finely characterizes the morphology of NaCl and of the BC aggregate.

Title Page

Abstract | Introduction

Conclusions | References

Tables | Figures

◄ | ►

◄ | ►

Back | Close

Full Screen / Esc

Printer-friendly Version

Interactive Discussion
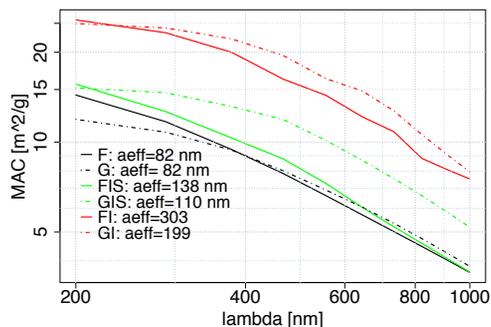
(a) *MAC for bare and internally mixed BC aggregates*
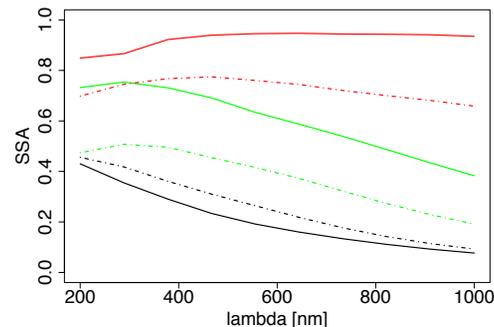
(b) *SSA for bare and internally mixed BC aggregates*

Fig. 7. (a) MAC in log-log scale and **(b)** SSA for different of bare BC and BC mixed with NaCl (see Table 2 and Figs. 5, 6). The refractive index (m) of BC ans NaCl has been considered constant in the spectral range between 200 and 1000 nm, where m_{BC} = 1.95–0.79i and m_{NaCl} = 1.5 and the density of BC (ρ_{BC}) is 1.8 g cm^{-3}. All the computed optical values are averaged over 64 particle orientations and satisfy the condition $|m|kd < 0.5$.

(a) *S11 at 466 nm* (b) *S11 at 733 nm*
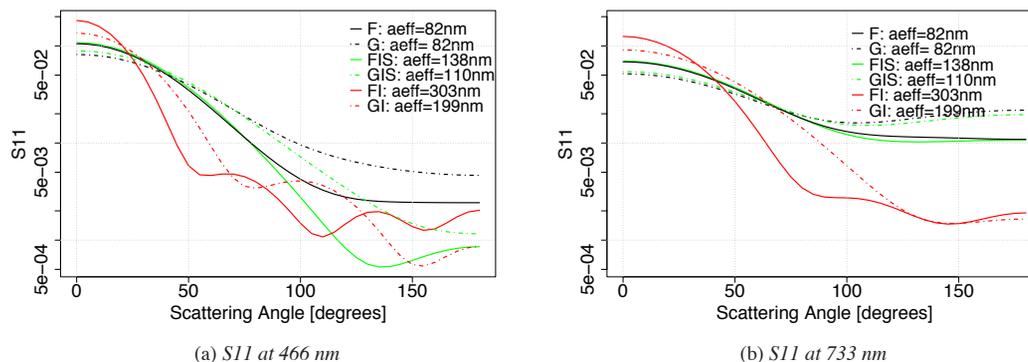
Fig. 8. Scattering phase function at 466 nm **(a)** and 733 nm **(b)**. Characteristics of the bare BC (cases F and G) and mixed BC-NaCl (cases FI, GI, FIS, and GIS) are described in Table 2 and Figs. 5, 6. A scattering angle of 0 degrees corresponds to radiation that is scattered in the forward direction (i.e., in the same direction as the incident radiation). A scattering angle of 180 degrees is backscattering. The coated aggregates are departing from the Rayleigh regime, and therefore display some angular variation, with forward scattering increasing.

(a) $\frac{-S12(\theta)}{S11(\theta)}$ *at 466 nm*

(b) $\frac{-S12(\theta)}{S11(\theta)}$ *at 733 nm*
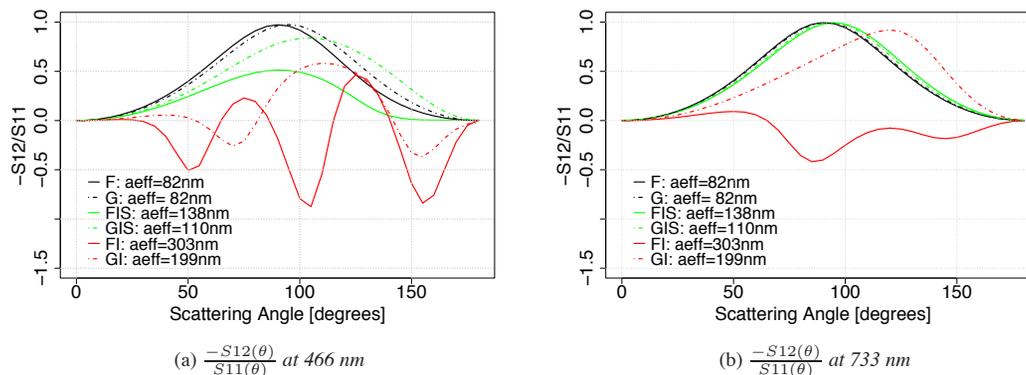
Fig. 9. Degree of linear polarization at 466 nm **(a)** and 733 nm **(b)**. Characteristics of the bare BC (cases F and G) and mixed BC-NaCl (cases FI, GI, FIS, and GIS) are described in Table 2 and Figs. 5, 6.